

1 Palaeotidal atlas of the UK for the last 2 10,000 years

3 Jon Hill¹

4 ¹Department of Environment and Geography, University of York. jon.hill@york.ac.uk

5 ABSTRACT

6 Over the past 10,000 years the UK has seen dramatic changes to its coastline due to sea-level
7 rise. Past changes in sea level can be estimated from analysis of sedimentary deposits,
8 including any microfossil assemblages found within. Once dated and the elevation is know,
9 these data become sea level index points (SLIPs). In recreating past sea level in this way there
10 is an implicit assumption of no change to the tidal regime, despite the fact we know this not to
11 be true. Here, I present modelling simulations of the tides of the UK for the past 10,000 years
12 based on current estimates of palaeoshorelines and bathymetry. I validate the tidal model on
13 modern tidal gauges using the 0 m contour as a shoreline as well as modern shoreline data,
14 before using the same model to create 30 day tidal simulations at 1,000 year intervals. This
15 palaeotidal atlas can be used to estimate both maximum tidal heights and tidal range which in
16 turn could be used to correct SLIPs. The results are consistent with previous estimates, despite
17 differences in estimated palaeobathymetry, boundary conditions and numerical technology
18 used. The tidal maps published will have a wide range of uses across Quaternary science.

19 Keywords: sea level, modelling, tides

20 Preprint submitted to Open Quaternary

21 INTRODUCTION

22 During the Holocene the Northwest European continental shelf sea has been transformed due
23 to sea-level rise due to deglaciation of the Fendo-Scandinavian ice sheet. Eustatic sea level has
24 risen some 130 m meters over the last 16,000 years with the majority of that change taking place
25 between 16,000 and 7,000 years (Lambeck et al., 2014). Not only does the rise vary temporally,
26 but due to isostatic rebound, relative sea level also varies spatially. This legacy is still relevant
27 today as the UK is experiencing differential rates of relative sea level rise with the south of the
28 UK experience much higher rates of relative sea level rise than the north (Shennan et al., 2018).

29 In order to assess past sea-level changes we need to find evidence of of where the sea level
30 was in the past. This evidence can be geomorphological (e.g. raised beaches), palaeontological
31 or sedimentological (e.g. marine sediments), archaeological (Shennan, 2015). By dating these
32 data, along with accurate measurements of location, the direction sea level is moving in and
33 height above/below modern mean water height (Shennan, 2015), the data can be terms a Sea
34 Level Index Point (SLIP). However, most SLIPS are data within the tidal range; that is they
35 represent some measure of water level, but not necessary the mean sea level (Hill, 2016; van de
36 Plassche, 1986). Therefore, to interpret the SLIP as mean sea level a tidal range is required.
37 Without any other information available, modern tidal ranges are used.

38 Previous numerical modelling studies have already established that tidal range can change
39 dramatically with changing sea levels. Previous studies have tended to focus on a smaller area,
40 e.g. the Wash or have used relatively coarse resolution of several km over the NW European shelf.
41 On of the first such model that used more than a simple M₂ forcing was that of Hinton (1992)

42 which modelled the southern North Sea coast of England using a 3 km regular grid. Hinton
 43 reconstructed palaeobathymetry simply by reducing or increasing sea level uniformly across the
 44 grid. Similar methods were employed by [Austin \(1991\)](#), who also examined the changes in tidal
 45 dissipation and tidal fronts. Models have since been developed that made use of GIA models,
 46 such as those of [Shennan and Horton \(2002\)](#) and [Neill et al. \(2010\)](#). The inclusion of a GIA
 47 model to estimate palaeobathymetric changes take into account the spatial nature of the changes.
 48 The most recent NW shelf model was that of [Ward et al. \(2016\)](#) which used a relatively coarse
 49 computational mesh of around 4.5 km (1/24 of a degree) and looked at changes to bed shear
 50 stress as well as tidal dynamics. All previous models show substantial changes in the Mean High
 51 Water Spring Tides and tidal range due to sea-level changes in the UK.

52 The result of palaeotidal models can be used to correct SLIPs for palaeo-tidal range. [Neill](#)
 53 [et al. \(2010\)](#) suggested this to be the case, but noted the inherent circularity of the problem –
 54 correcting SLIPs alters the GIA model, which in turn alters the palaeobathymetry and then the
 55 tidal range estimates. [Neill et al. \(2010\)](#) suggest a procedure whereby some SLIPs are held
 56 back from the GIA model used to define the palaeobathymetry of the tidal model to provide a
 57 verification-calibration study. [Ward et al. \(2016\)](#) agree that this methodology could be useful
 58 and also that higher resolution models are better suited to this as SLIPs are often found near
 59 coastlines or in estuaries.

60 Here, I use multiscale modelling on an unstructured mesh with resolution varying from
 61 20 km to 1.5 km around the coastlines, with palaeobathymetry derived from the 2011 GIA
 62 modelling of [Bradley et al. \(2011\)](#). This is the first time a multiscale approach has been used in
 63 this way and that all model outputs made freely available for further study. Unstructured mesh
 64 models have particular advantages when modelling complex coastlines and bathymetries as they
 65 avoid the ‘staircase effect’ ([Wells et al., 2005a](#)) typically seen in structured mesh models (Fig. 1).
 66 Increasing resolution to where it is needed (e.g. coastlines or rapid changes in bathymetry) means
 67 that the accuracy of a higher resolution model is obtained whilst minimising computational
 68 expense.

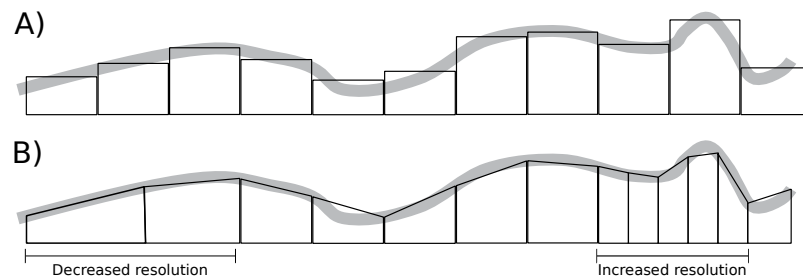


Figure 1. Example of the ‘staircase effect’ when modelling bathymetry. The thick grey line is the actual bathymetry. In the structured grid model (A) this is represented as a value in a cell, resulting in sharp edges where bathymetry changes more quickly than the mesh size can resolve. In contrast an unstructured grid model can use linear functions within cells (or indeed higher order functions) and change resolution where needed. Unstructured mesh models typically take longer to solve for the same resolution, however.

69 In this paper, I outline the details of the model set-up used before validating this model on
 70 the modern UK tidal gauge data. I then detail the set up for the palaeotidal models and then
 71 present results of the tidal atlas at 1,000 year intervals. Results are shown for a number output
 72 parameters including tidal stratification estimates. I conclude by discussing the implications
 73 of this study in terms of correcting the European SLIP database and how we could avoid the

74 circularity problem.

75 METHODS AND MATERIALS

76 The palaeotides were calculated using the Fluidity model, which is a highly flexible finite
77 element/control volume modelling framework which allows for the numerical solution of a
78 number of equation sets (Piggott et al., 2008) and has been used in a variety of tidal studies,
79 including both modern and ancient tides on regional and global scales (Wells et al., 2005b,a,
80 2007, 2010; Martin-Short et al., 2015; Collins et al., 2017, 2018). One of the major advantages
81 of Fluidity is the use of a multiscale mesh, which can resolve fine-scale details even in a regional
82 setting using resolution down to metre-scale (Martin-Short et al., 2015).

83 Fluidity

Here, the depth-averaged shallow water equations are solved in a rotating reference frame in non-conservative form:

$$\begin{aligned} \frac{\partial u}{\partial t} + u \cdot \nabla u + fu^T - \nabla v \left[\nabla u + (\nabla u)^T \right] + g \nabla \eta &= -c_b \frac{\|u\|u}{H}, \\ \frac{\partial \eta}{\partial t} + \nabla \cdot (Hu) &= 0, \end{aligned} \quad (1)$$

84 where u is the 2D, depth-averaged velocity vector, t represents time, η is the free surface
85 perturbation, H is the total water depth, and ν is the kinematic viscosity. The Coriolis term,
86 fu^T , consists of u^T , the velocity vector rotated counter-clockwise over 90° , and $f = 2\Omega \sin(\zeta)$,
87 with Ω the angular frequency of Earth's rotation and ζ the latitude. The dimensionless friction
88 coefficient c_b represent respectively the background bottom drag (assumed constant here).

89 The equations (1) are discretised on a mixed finite element pair, with a continuous Galerkin,
90 piecewise quadratic formulation for the free surface (P2) and a piecewise linear discontinuous
91 Galerkin approximation (P1_{DG}) for velocity. The resulting P1_{DG}P2 velocity/free-surface dis-
92 cretisation has a number of desirable properties described fully in Cotter et al. (2009a,b); Cotter
93 and Ham (2011). In addition to the discretisation of the linear shallow water terms described
94 therein, we employ a standard P1_{DG}-discretisation with upwind fluxes and slope limiting for the
95 advection term and the Compact Discontinuous Galerkin scheme Peraire and Persson (2008), for
96 the viscosity term.

97 A two-level θ method is employed for time-integration, combined with explicit subcycling
98 for the advection step. Here $\theta = 0.53$, which is close to the Crank-Nicolson scheme, and
99 therefore minimises wave dissipation whilst maintaining stability. Two Picard iterations per
100 time-step are used to linearise the nonlinearity in the advection and friction terms. Finally, the
101 linear discretised systems are solved using iterative sparse linear solvers available in PETSc
102 Balay et al. (2018). More details on the spatial and temporal discretisations available in Fluidity
103 are described in Imperial College London AMCG (2015) and Piggott et al. (2008).

104 Model setup

105 The model domain consisted of the entire NW European continental shelf, bordered by coastlines
106 and the Danish Straits (Fig. 2). For present day simulations two coastlines types were modelled.
107 One using the high resolution GSHHS coastline dataset (Wessel and Smith, 1996), the other
108 using the 0 m contour. For each timeslice from 1 ka to 10 ka, modern bathymetry derived from
109 GEBCO 2014 (Weatherall et al., 2015) was adjusted according to the glacio-isostatic adjustment
110 (GIA) model of Bradley et al. (2011) to create a palaeobathymetry. For each palaeobathymetry,
111 a coastline derived from the 0 m contour was created, which served as a numerical boundary.
112 This was trimmed to meet the western boundary and the boundary at the Denmark Straits. The

113 mesh resolution varied with highest resolution along coastlines (1.5 km triangles), 3 km along
 114 other boundaries and 25 km between 50 and 100 km away from a boundary. In addition, a mesh
 115 metric based on idealised wave celerity increased resolution in deeper water where the tidal wave
 116 moves quickest (Lambrechts et al., 2008) via:

$$50000.0 * \sqrt{\frac{10.0}{h}} \quad (2)$$

117 where h is the water depth. All points on the coastlines and boundaries were joined using a
 118 B-spline curve to produce a smooth boundary for the final mesh. All meshes were constructed in
 119 (qmesh) (Avdis et al., 2018).

120 The coastlines and sea bed were set to no-normal flow with a Manning quadratic drag
 121 formulation applied with a drag coefficient of 0.025. The open boundary was forced via free
 122 surface using the FES2014 data (Lyard et al., 2006). A short boundary section between coastline
 123 and the open boundary was set to a no-slip boundary. Bathymetry was ‘dredged’ to ensure the
 124 minimum water depth was 6 m to prevent stability issues as the model does not include wetting
 125 and drying. Each model was spun up for 30 days, before then being run for another 30 days. The
 126 final 30 days were used for all subsequent analyses.

127 Modern validation

128 To assess model performance I compared the model against tide gauge data from around the UK
 129 using the two different methods of coastlines generation for the present day (0 m contour and
 130 GSHHS). The two modern models were forced along the boundary of the continental shelf using
 131 FES 2014 data and eight principle tidal components, M_2 , S_2 , N_2 , K_2 , O_1 , Q_1 , K_1 , and P_1 . The
 132 constituents M_2 and S_2 are the dominant components on the NW European continental shelf.
 133 The model was run for a total of 60 days, with the first 30 days considered as ‘spin-up’. Free
 134 surface height data were then analysed at each tidal gauge location to produce model estimates
 135 of M_2 , S_2 , K_1 , and O_1 amplitude and phases and compared to the data from tide gauges. To
 136 compare the model against the tide gauges we use the method of Cummins and Thupaki (2017),
 137 whereby error, ξ is calculated over the L tidal gauges as:

$$\xi = L^{-1} \sum D_L \quad (3)$$

$$D_L = \left[\frac{1}{2} (A_o^2 + A_m^2) - A_o A_m \cos(\phi_o - \phi_m) \right]^{\frac{1}{2}} \quad (4)$$

138 where A_m is the modelled amplitude, A_o is the observed amplitude, ϕ_o is the observed phase and
 139 ϕ_m is the modelled phase, at each tidal gauge location. A separate D is calculated for each tidal
 140 constituent modelled.

141 In the modern day, the mode has an error of 0.27 - 0.39 cm for M_2 and 0.06 - 0.03 cm for
 142 S_2 across 40 or 41 tidal stations (0 m contour or GSHHS coastline respectively), corresponding
 143 to a 0.14 - 0.22 and 0.06 - 0.09 % error respectively according to equation 4. Fluidity appears
 144 to slightly under predict the O_1 component and over predict the K_1 component compared to
 145 tide gauges at higher amplitudes, but the mean semi-diurnal components show an excellent
 146 agreement (Fig. 3). Both GSHHS and 0 m contour derived coastlines perform well overall.

147 The spatial distribution of the M_2 tide and tidal range matches previous modelling studies
 148 (Fig. 4). A major control on sediment movement in the NW European shelf sea are tidal currents
 149 (Fig 4). Ward et al. (2015) developed a proxy for tidally induced bed shear stress and sediment
 150 grain size which attempts to account for additional controls on sediment movement such as

Model	M ₂ error	S ₂ error	K ₁ error	O ₁ error	No. Stations
GSHHS (%)	0.22%	0.06%	0.07%	0.08%	41
GSHHS (cm)	0.39	0.03	0.07	0.08	41
0m (%)	0.14%	0.09%	0.82%	0.87%	40
0m (cm)	0.27	0.06	0.08	0.08	40

151 waves and storm events. Here, I use this proxy across the whole NW continental shelf to derive
 152 grain size estimates from tidal bed shear stress. The modelling results (Fig. 4) show the North
 153 Sea grain size as generally coarse sand, fining to very fine sand or less towards Norway. The
 154 Celtic Sea is dominated by medium to coarse sand grains, with a ribbon of very coarse sand
 155 running south from Scotland, through the Isle of Mann towards the Irish coast, before turning
 156 more easterly towards Wales. Similarly, the Severn Estuary is also coarse sand. The English
 157 channel is also dominated by coarse sands with some Gravel patches on the French coast. The
 158 coarse sediment is discontinuous in the easterly direction with patches of medium sand. The
 159 results in the Celtic Sea are entirely consistent with [Ward et al. \(2015\)](#) as well as observations by
 160 [Bockelmann et al. \(2018\)](#).

161 PALAEO-TIDAL CHANGES

162 The M₂ tidal component is the dominant component over most of the of NW European continental
 163 shelf. At 10 ka, an amphidromic point is situated near the palaeo-coastline in the North Sea
 164 (Fig. 5). There is a further point further north near Norway. At this time there is a significant
 165 reduction in M₂ amplitude across the whole seaway. When the land bridge between the UK and
 166 mainland Europe forms around 9 ka, these points become separated by the land bridge with
 167 a single amphidromic point in the English channel and two to the north and south of Dogger
 168 Bank respectively. The shallowing of the Dogger Bank area in the southern North Sea creates
 169 additional amphidromic points in the area which then precipitates a reduction in M₂ amplitude
 170 in the English Channel. By the time Dogger Bank becomes emergent at around 8 ka, there are
 171 complex tidal dynamics in the southern area of the North Sea, with four amphidromic points
 172 occurring in the area. At 7 ka the amphidromic points shift towards the modern configuration,
 173 with an additional point off the palaeo-coast of Denmark. Between 6 and 0 ka there is no major
 174 shift in the amphidromic points and moderate changes in M₂ tidal amplitude. There is, however,
 175 a minor shift at 4ka. The amphidromic point shifts towards the UK coast from the east of the
 176 North Sea at this time. This then reduces the M₂ amplitude slightly on the eastern coast of
 177 the UK. The driver for this appears to be sea-level change on the north coast of Europe. In
 178 the modern, the Severn Estuary and Brittany coast experience high tidal ranges due to the M₂
 179 component. The modern North Sea shows amphidromic points (points where phase contours
 180 converge) near the Danish coast and in the northern part of the English Channel.

181 Comparing to previous studies ([Neill et al., 2010](#)) and ([Ward et al., 2016](#)), the estimates
 182 presented here show very similar spatial features as well as absolute values of M₂ tidal amplitude
 183 and phase. There are minor variations in the location of amphidromic points. The models results
 184 here show an additional amphidromal points off the coast of Norway at 10 ka compared to the
 185 results of [Neill et al. \(2010\)](#) and ([Ward et al., 2016](#)). There is very little difference in the M₂
 186 amplitudes, however. At 8 ka all models show a complex set of amphidromic points in the
 187 southern North Sea, with similar patterns of M₂ amplitude.

188 These changes in the M₂ tide causes shifts in tidal range over the time period studies (Fig.
 189 6). The tidal range at 10 ka is much lower than modern day due to the much lower sea level.
 190 At 9 ka there is also an increase in tidal range in the Celtic Sea and the Severn Estuary closer
 191 to modern values. When the English Channel opens at 8 ka the tidal range is consistent with

192 modern day. The tidal range stays generally consistent to the modern day ranges, apart from
 193 a minor change around 4 ka due to the changes in M_2 described above. These results mirror
 194 those of Neill et al. (2010), which show a rapid reduction of tidal range between 0 and 10 ka
 195 with most of that change taking place at some point between 6 ka and 10 ka. However, the tidal
 196 range estimates presented here at 10 ka are slightly lower than that of Neill et al. (2010).

197 Tidal mixing

198 Tidal mixing occurs when the tidal currents are strong enough to induce turbulence via shear on
 199 the sea bed. There is therefore a relationship between water depth, tidal velocity and mixing in
 200 the water column which can be described using the Hunter-Simpson parameter, H_s ,

$$H_s = \log_{10} \frac{h}{u^3} \quad (5)$$

201 where h is the water depth (m) and u is the mean of tidal velocity magnitude (m/s) (Simpson and
 202 Hunter, 1974). Where tidal mixing occurs, it can flux nutrients from depth into the photic zone,
 203 thereby increasing primary productivity. This mixing occurs in the summer months when the
 204 solar radiation is sufficiently strong to induce stratification. Simpson and Hunter (1974) cite a
 205 value of between 1.5 and 2.0 for eq. 5 for where the transition between mixed and stratified water
 206 occurs; the tidal front, which has been confirmed with observations in the Celtic Sea (Simpson,
 207 1976). Fig. 7 shows the shift in the tidal fronts through time. For the period 10 ka to 7 ka
 208 there are widespread mixed areas in the English Channel and Southern North Sea. As sea level
 209 rises and becomes similar to modern day these fronts become very similar to those found today
 210 (Pingree and Griffiths, 1978), apart from those in the Celtic and Irish Seas. Those fronts develop
 211 around 6ka, but are absent at 4 - 1 ka.

212 Sediment grain size changes

213 Changes in sediment grain size largely follow the changes in tidal range (Fig. 8). Generally
 214 there is a increase in grain size deposited with time, with fine grains dominating 10 ka and areas
 215 becoming dramatically coarser by around 7 ka and then stabilising. The largest changes occur
 216 between 10 ka and 7 ka in the English channel. In the modern there are two main areas of very
 217 coarse sand deposition in the English channel - on in the narrow seaway between England and
 218 France and a large area between the south cost of England and Brittany. These a re largely
 219 stable until around 7 ka when the northern patch shrinks whilst the southern area grows. As the
 220 English Channel shrinks this southern patch of coarse sediment shifts southwards and eventually
 221 decreases in area by 10 ka. These results are similar to the tidal bed shear stress calculated by
 222 Neill et al. (2010) and Ward et al. (2016), though as with the tidal characteristics there are minor
 223 differences in places.

224 DISCUSSION

225 In order to calculate sea level since the Last Glacial Maximum we must first find data that
 226 indicate past sea level. These data points are located within a tidal range, however; so in order
 227 to place past mean sea level an estimate of past tidal range is required (Shennan, 2015). It is
 228 important to understand past sea level changes as they relate directly to our estimates of the
 229 amount of water sequester by ice sheets during the Last Glacial maximum Clark and Tarasov
 230 (2014) and what drives local, regional and global sea level chnage through time (Shennan et al.,
 231 2018). Here, I present calculations of past tides of the NW European continental shelf using a
 232 finite element model on a multi-scale unstructured mesh. The output of these model simulations
 233 are available for other researchers to use.

234 The tidal characteristics of the European continental shelf show major changes over the past
235 10,000 years. Most of those changes are associated with the flooding in the southern North Sea
236 from 10 ka to 7 ka. From 7 ka to the present day most tidal properties show little variation. The
237 exception to this is at 4 ka. At this time the amphidromic point for the M_2 tide shifts westwards
238 in the southern North Sea moving the corresponding M_2 low amplitude with it. This in turn
239 alters tidal range and bed shear stresses in the region. By 3 ka the amphidromic point shifts
240 eastward again, closer to the modern day location.

241 The shifts in tidal characteristic also have implications in the primary productivity potential
242 of the European shelf. From 10 ka to 7 ka there was a much larger mixed region in the English
243 Channel with associated tidal fronts. These are associated with both shallower water and higher
244 tidal velocities. These fronts would have increased the primary productivity in the region as tidal
245 fronts are a significant percentage of primary productivity in the modern North Sea (Heath and
246 Beare, 2008). This in turn has implications for changes in the biogeochemistry of the North
247 Sea since the Last Glacial Maximum. The present day North Sea is thought to store around 250
248 MT of Particulate Organic Matter (POC) in the top 10 cm of sediment (Diesing et al., 2017).
249 Given that the North Atlantic biological pump increased the draw down of carbon during the
250 Last Glacial Maximum (Yu et al., 2019), the increased number of tidal fronts may have had an
251 impact on the POC stored in North Sea sediments.

252 The model results presented here have a number of limitations. Firstly, the boundary
253 forcing along the continental shelf are derived from modern data with no corrections for global
254 palaeobathymetric changes. This is in contrast to both Neill et al. (2010) and Ward et al. (2016).
255 As the ice sheets in the northern hemisphere grew, they caused changes in the global tidal
256 dynamics. However, the tidal forcing was still strong in this region and broadly comparable to
257 modern tides at least until 10 ka, based on previous modelling of global tides (Uehara et al.,
258 2006). Future work will use global tidal models to estimate the tidal boundary forcing on
259 global palaeobathymetries to enable simulations to be carried out for reconstructions older than
260 10 ka. Second, the model also lacks inundation of low-lying land due to tidal movement with
261 bathymetry 'dredged' to a minimum of 6 m water depth. This is a particular problem in estuaries
262 and where most SLIP data are collected. This is similar to both Neill et al. (2010) and Ward et al.
263 (2016) as neither used any wetting and drying algorithms. Whilst the modelled tidal range is not
264 significantly affected the tidal range must instead be taken from a nearby point rather than the
265 precise location of the SLIP. Future work will correct this by adding inundation and increase the
266 spatial resolution around the coast.

267 The results presented here form only part of the solution for correcting SLIPs for palaeo-tidal
268 range. Once a SLIP is corrected for temporal variations in tidal range, the GIA models then
269 need correcting as they use SLIPs as a constraint, which in turn alters the palaeobathymetry on
270 which the tidal model is based. This presents something of a circular problem. Neill et al. (2010)
271 proposed a methodology whereby some SLIPs are held back from a GIA model to provide a
272 validation-calibration test. However, here, I have used a different palaeobathymetry to Neill et al.
273 (2010) and modern forcing as opposed to palaeotidal estimates. Similarly, Ward et al. (2016)
274 used updated GIA models (same as this work) and a higher model resolution than Neill et al.
275 (2010). Despite these minor differences in boundary forcing, palaeobathymetric reconstructions,
276 and numerical implementations, our estimates of tidal range changes are very similar. This is
277 encouraging as it means that tidal range estimates are not overly sensitive to minor variations in
278 tidal forcing or palaeobathymetric estimates. It should therefore be possible to correct SLIPs
279 for tidal range, alter the palaeobathymetry and proceed in an iterative fashion until there are no
280 changes to the tidal estimates – in essence convergence onto our best estimate. Making use of
281 modern numerical techniques such as adjoint solvers would aid in estimating the sensitivity of the
282 tidal model to errors in palaeobathymetry. In turn the sensitivity and error across multiple models

283 and bathymetric estimates could be used in a Bayesian framework similar to that proposed by
284 (Cahill et al., 2016). It would then be possible to account for uncertainty and sensitivity in the
285 SLIP height (including tidal range corrections and the uncertainties within those) and the dating
286 method when deriving sea level estimates.

287 CONCLUSIONS

288 The results published here form a palaeotidal database made freely available for future researchers.
289 The outputs of the model shows significant changes to tidal range, tidal sediment distribution
290 and the tidal components on the NW European shelf area. These data are the first derived on an
291 unstructured mesh model where the mesh resolution of the model can vary spatially, allowing
292 focusing of results in areas of interest (here the coastline) whilst minimising computations time.
293 Unstructured meshes also reproduce bathymetry and coastlines without staircase effects. This is
294 an advance over previous modelling studies that used relatively coarse rectilinear grids.

295 DATA AVAILABILITY

296 Each time slice is available as a NetCDF file which contains tidal amplitudes and phases for
297 each tidal component, maximum and mean bed shear stress and velocity vectors, along with
298 a simple R script to extract nearest data from a list of points. These are available via: DOI:
299 [10.6084/m9.figshare.6993956](https://doi.org/10.6084/m9.figshare.6993956).

300 ACKNOWLEDGEMENTS

301 This project was undertaken on the Viking Cluster, which is a high performance compute facility
302 provided by the University of York. I am grateful for computational support from the University
303 of York High Performance Computing service, Viking and the Research Computing team. I
304 would also like to thank Graham Rush and Fiona Hibbert (University of York) for commenting
305 on drafts of the manuscript.

306 REFERENCES

- 307 Austin, R. M. (1991). Modelling Holocene tides on the NW European continental shelf. *Terra*
308 *Nova*, 3(3):276–288.
- 309 Avdis, A., Candy, A. S., Hill, J., Kramer, S. C., and Piggott, M. D. (2018). Efficient unstructured
310 mesh generation for marine renewable energy applications. *Renewable Energy*, 116:842–856.
- 311 Balay, S., Abhyankar, S., Adams, M. F., Brown, J., Brune, P., Buschelman, K., Dalcin, L., Dener,
312 A., Eijkhout, V., Gropp, W. D., Kaushik, D., Knepley, M. G., May, D. A., McInnes, L. C.,
313 Mills, R. T., Munson, T., Rupp, K., Sanan, P., Smith, B. F., Zampini, S., Zhang, H., and Zhang,
314 H. (2018). PETSc users manual. Technical Report ANL-95/11 - Revision 3.9, Argonne
315 National Laboratory.
- 316 Bockelmann, F.-D., Puls, W., Kleeberg, U., Müller, D., and Emeis, K.-C. (2018). Mapping mud
317 content and median grain-size of North Sea sediments – A geostatistical approach. *Marine*
318 *geology*, 397:60–71.
- 319 Bradley, S. L., Milne, G. A., Shennan, I., and Edwards, R. (2011). An improved glacial isostatic
320 adjustment model for the British Isles. *Journal of Quaternary Science*, 26(5):541–552.
- 321 Cahill, N., Kemp, A. C., Horton, B. P., and Parnell, A. C. (2016). A Bayesian hierarchical model
322 for reconstructing relative sea level: from raw data to rates of change. *Climate of the Past*,
323 12(2):525–542.
- 324 Clark, P. U. and Tarasov, L. (2014). Closing the sea level budget at the Last Glacial Maxi-
325 mum. *Proceedings of the National Academy of Sciences of the United States of America*,
326 111(45):15861–15862.

- 327 Collins, D. S., Avdis, A., Allison, P. A., Johnson, H. D., Hill, J., and Piggott, M. D. (2018).
328 Controls on tidal sedimentation and preservation: insights from numerical tidal modelling in
329 the Late Oligocene–Miocene South China Sea, Southeast Asia. *Sedimentology*.
- 330 Collins, D. S., Avdis, A., Allison, P. A., Johnson, H. D., Hill, J., Piggott, M. D., Amir Hassan,
331 M. H., and Damit, A. R. (2017). Tidal dynamics and mangrove carbon sequestration during
332 the Oligo–Miocene in the South China Sea. *Nature communications*, 8:ncomms15698.
- 333 Cotter, C. J. and Ham, D. A. (2011). Numerical wave propagation for the triangular P1DG–P2
334 finite element pair. *Journal of computational physics*, 230(8):2806–2820.
- 335 Cotter, C. J., Ham, D. A., and Pain, C. C. (2009a). A mixed discontinuous/continuous finite
336 element pair for shallow-water ocean modelling. *Ocean Modelling*, 26:86–90.
- 337 Cotter, C. J., Ham, D. A., Pain, C. C., and Sebastian, R. (2009b). LBB stability of a mixed
338 Galerkin finite element pair for fluid flow simulations. *Journal of computational physics*,
339 228(2):336–348.
- 340 Cummins, P. F. and Thupaki, P. (2017). A note on evaluating model tidal currents against
341 observations. *Continental shelf research*.
- 342 Diesing, M., Kröger, S., Parker, R., Jenkins, C., Mason, C., and Weston, K. (2017). Predicting the
343 standing stock of organic carbon in surface sediments of the North-West European continental
344 shelf. *Biogeochemistry*, 135(1):183–200.
- 345 Heath, M. R. and Beare, D. J. (2008). New primary production in northwest European shelf seas,
346 1960–2003. *Marine ecology progress series*, 363:183–203.
- 347 Hill, D. F. (2016). Spatial and Temporal Variability in Tidal Range: Evidence, Causes, and
348 Effects. *Current Climate Change Reports*, 2(4):232–241.
- 349 Hinton, A. C. (1992). Palaeotidal changes within the area of the Wash during the Holocene.
350 *Proceedings of the Geologists' Association. Geologists' Association*, 103:259–272.
- 351 Imperial College London AMCG (2015). Fluidity manual v4.1.12. *figshare*.
- 352 Lambeck, K., Rouby, H., Purcell, A., Sun, Y., and Sambridge, M. (2014). Sea level and global
353 ice volumes from the Last Glacial Maximum to the Holocene. *Proceedings of the National
354 Academy of Sciences of the United States of America*, 111(43):15296–15303.
- 355 Lambrechts, J., Comblen, R., Legat, V., Geuzaine, C., and Remacle, J.-F. (2008). Multiscale
356 mesh generation on the sphere. *Ocean Dynamics*, 58(5-6):461–473.
- 357 Lyard, F., Lefevre, F., Letellier, T., and Francis, O. (2006). Modelling the global ocean tides:
358 modern insights from FES2004. *Ocean Dynamics*, 56(5):394–415.
- 359 Martin-Short, R., Hill, J., Kramer, S. C., Avdis, A., Allison, P. A., and Piggott, M. D. (2015).
360 Tidal resource extraction in the Pentland Firth, UK: Potential impacts on flow regime and
361 sediment transport in the Inner Sound of Stroma. *Renewable Energy*, 76(0):596–607.
- 362 Neill, S. P., Scourse, J. D., and Uehara, K. (2010). Evolution of bed shear stress distribution
363 over the northwest European shelf seas during the last 12,000 years. *Ocean Dynamics*,
364 60(5):1139–1156.
- 365 Peraire, J. and Persson, P. (2008). The Compact Discontinuous Galerkin (CDG) Method for
366 Elliptic Problems. *SIAM Journal of Scientific Computing*, 30(4):1806–1824.
- 367 Piggott, M. D., Gorman, G. J., Pain, C. C., Allison, P. A., Candy, A. S., Martin, B. T., and
368 Wells, M. R. (2008). A new computational framework for multi-scale ocean modelling based
369 on adapting unstructured meshes. *International Journal for Numerical Methods in Fluids*,
370 56(8):1003–1015.
- 371 Pingree, R. D. and Griffiths, D. K. (1978). Tidal fronts on the shelf seas around the British Isles.
372 *Journal of geophysical research*, 83(C9):4615–4622.
- 373 Shennan, I. (2015). Handbook of sea-level research: framing research questions. In Shennan, I.,
374 Long, A. J., and Horton, B. P., editors, *Handbook of Sea-Level Research*, volume 113, pages
375 3–25. John Wiley & Sons, Ltd, Chichester, UK.

- 376 Shennan, I., Bradley, S. L., and Edwards, R. (2018). Relative sea-level changes and crustal
377 movements in Britain and Ireland since the Last Glacial Maximum. *Quaternary science*
378 *reviews*, 188:143–159.
- 379 Shennan, I. and Horton, B. (2002). Holocene land-and sea-level changes in Great Britain. *Journal*
380 *of Quaternary Science: Published for the Quaternary Research Association*, 17(5-6):511–526.
- 381 Simpson, J. H. (1976). A boundary front in the summer regime of the Celtic Sea. *Estuarine and*
382 *Coastal Marine Science*, 4(1):71–81.
- 383 Simpson, J. H. and Hunter, J. R. (1974). Fronts in the Irish Sea. *Nature*, 250(5465):404–406.
- 384 Uehara, K., Scourse, J. D., Horsburgh, K. J., Lambeck, K., and Purcell, A. P. (2006). Tidal
385 evolution of the northwest European shelf seas from the Last Glacial Maximum to the present.
386 *Journal of geophysical research*, 111(C9):235.
- 387 van de Plassche, O., editor (1986). *Sea-Level Research*. Springer Netherlands, Dordrecht.
- 388 Ward, S. L., Neill, S. P., Scourse, J. D., Bradley, S. L., and Uehara, K. (2016). Sensitivity of
389 palaeotidal models of the northwest European shelf seas to glacial isostatic adjustment since
390 the Last Glacial Maximum. *Quaternary science reviews*, 151:198–211.
- 391 Ward, S. L., Neill, S. P., Van Landeghem, K. J. J., and Scourse, J. D. (2015). Classifying seabed
392 sediment type using simulated tidal-induced bed shear stress. *Marine geology*, 367:94–104.
- 393 Weatherall, P., Marks, K. M., Jakobsson, M., Schmitt, T., Tani, S., Arndt, J. E., Rovere, M.,
394 Chayes, D., Ferrini, V., and Wigley, R. (2015). A new digital bathymetric model of the world's
395 oceans. *Life support & biosphere science: international journal of earth space*, 2(8):331–345.
- 396 Wells, M. R., Allison, P. A., Hampson, G. J., Piggott, M. D., and Pain, C. C. (2005a). Mod-
397 elling ancient tides: the Upper Carboniferous epi-continental seaway of Northwest Europe.
398 *Sedimentology*, 52(4):715–735.
- 399 Wells, M. R., Allison, P. A., Piggott, M. D., Gorman, G. J., Hampson, G. J., Pain, C. C., and Fang,
400 F. (2007). Numerical Modeling of Tides in the Late Pennsylvanian Midcontinent Seaway of
401 North America with Implications for Hydrography and Sedimentation. *Journal of Sedimentary*
402 *Research*, 77(10):843–865.
- 403 Wells, M. R., Allison, P. A., Piggott, M. D., Hampson, G. J., Pain, C. C., and Gorman, G. J.
404 (2010). Tidal Modeling of an Ancient Tide-Dominated Seaway, Part 1: Model Validation and
405 Application to Global Early Cretaceous (Aptian) Tides. *Journal of Sedimentary Research*,
406 80(5):393–410.
- 407 Wells, M. R., Allison, P. A., Piggott, M. D., Pain, C. C., Hampson, G. J., and DE Oliveira, C.
408 R. E. (2005b). Large sea, small tides: the Late Carboniferous seaway of NW Europe. *Journal*
409 *of the Geological Society*, 162(3):417–420.
- 410 Wessel, P. and Smith, W. H. F. (1996). A Global Self-consistent, Hierarchical, High-resolution
411 Shoreline Database. *Journal of geophysical research*, 101(B4):8741–8743.
- 412 Yu, J., Menviel, L., Jin, Z. D., Thornalley, D. J. R., Foster, G. L., Rohling, E. J., McCave,
413 I. N., McManus, J. F., Dai, Y., Ren, H., He, F., Zhang, F., Chen, P. J., and Roberts, A. P.
414 (2019). More efficient North Atlantic carbon pump during the Last Glacial Maximum. *Nature*
415 *communications*, 10(1):2170.

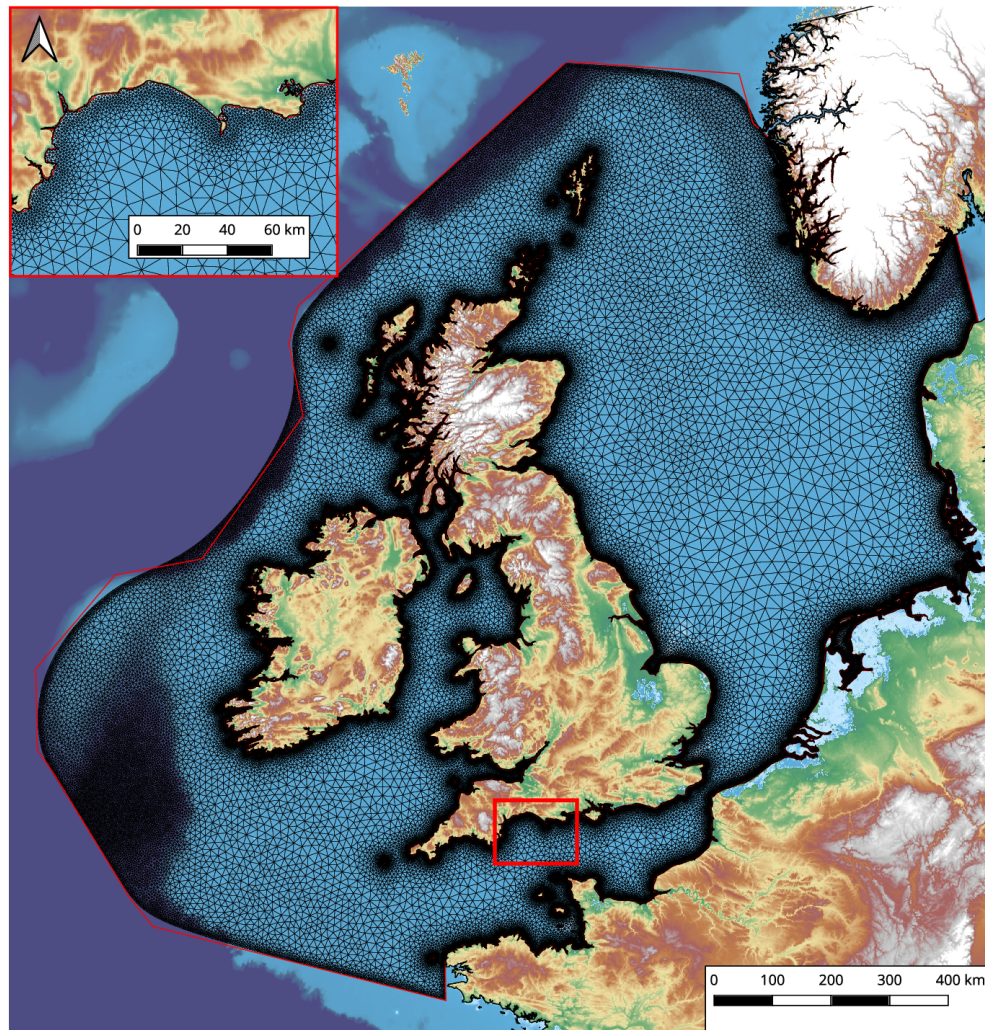


Figure 2. Modern multiscale mesh using GSHHS coastlines (high resolution). Mesh resolution is smallest around coastlines and deeper water. Red line shows the coastline from GSHHS, black is the mesh, and colours show height from the GEBCO bathymetry/topography. A close-up of the south coast of England is shown to highlight the mesh resolution change with respect to the coastline.

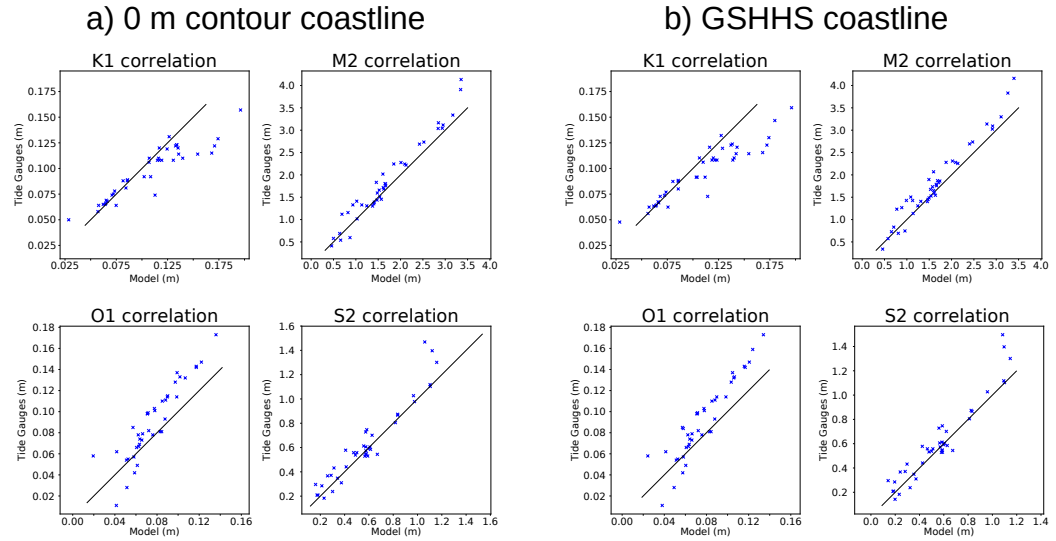


Figure 3. Cross plot of amplitudes generated from Fluidity against tide gauges for four main tidal components using either the 0 m contour (a) or high resolution GSHHS data (b) as the coastline.

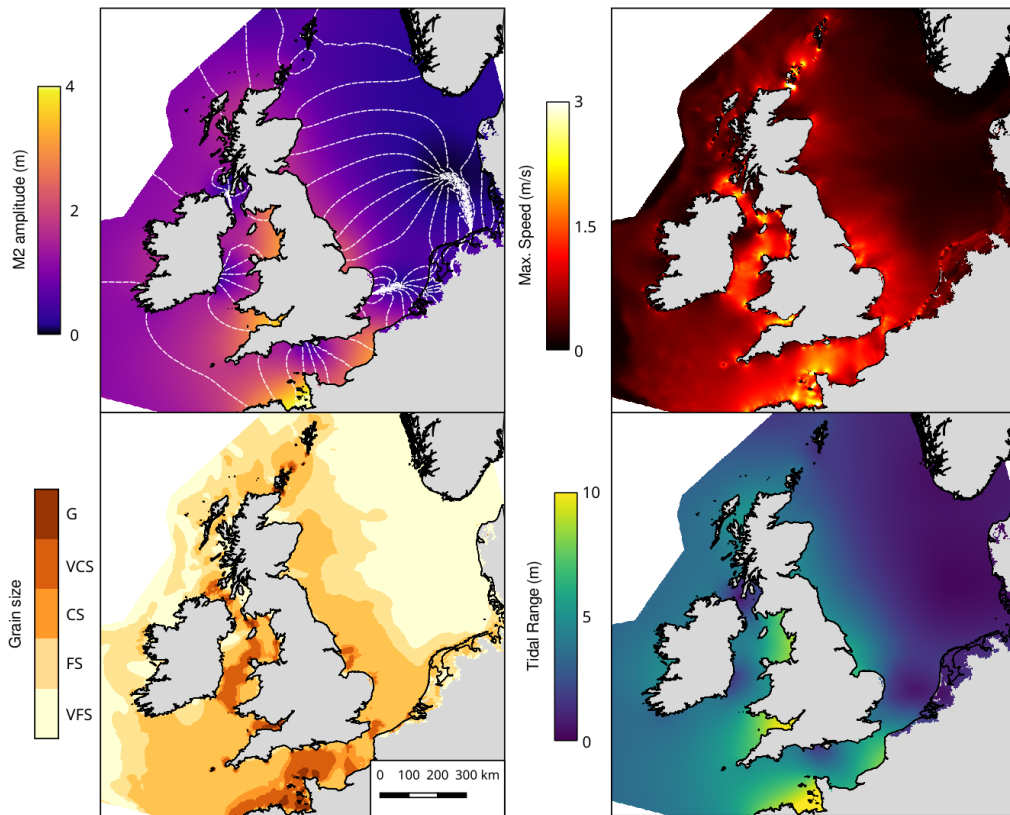


Figure 4. Tidal properties of the present day. Top left: M₂ amplitude and phase. Top right: maximum speed over the 30 day simulation. Bottom left: grain size derived from maximum bed shear stress. Bottom right: tidal range.

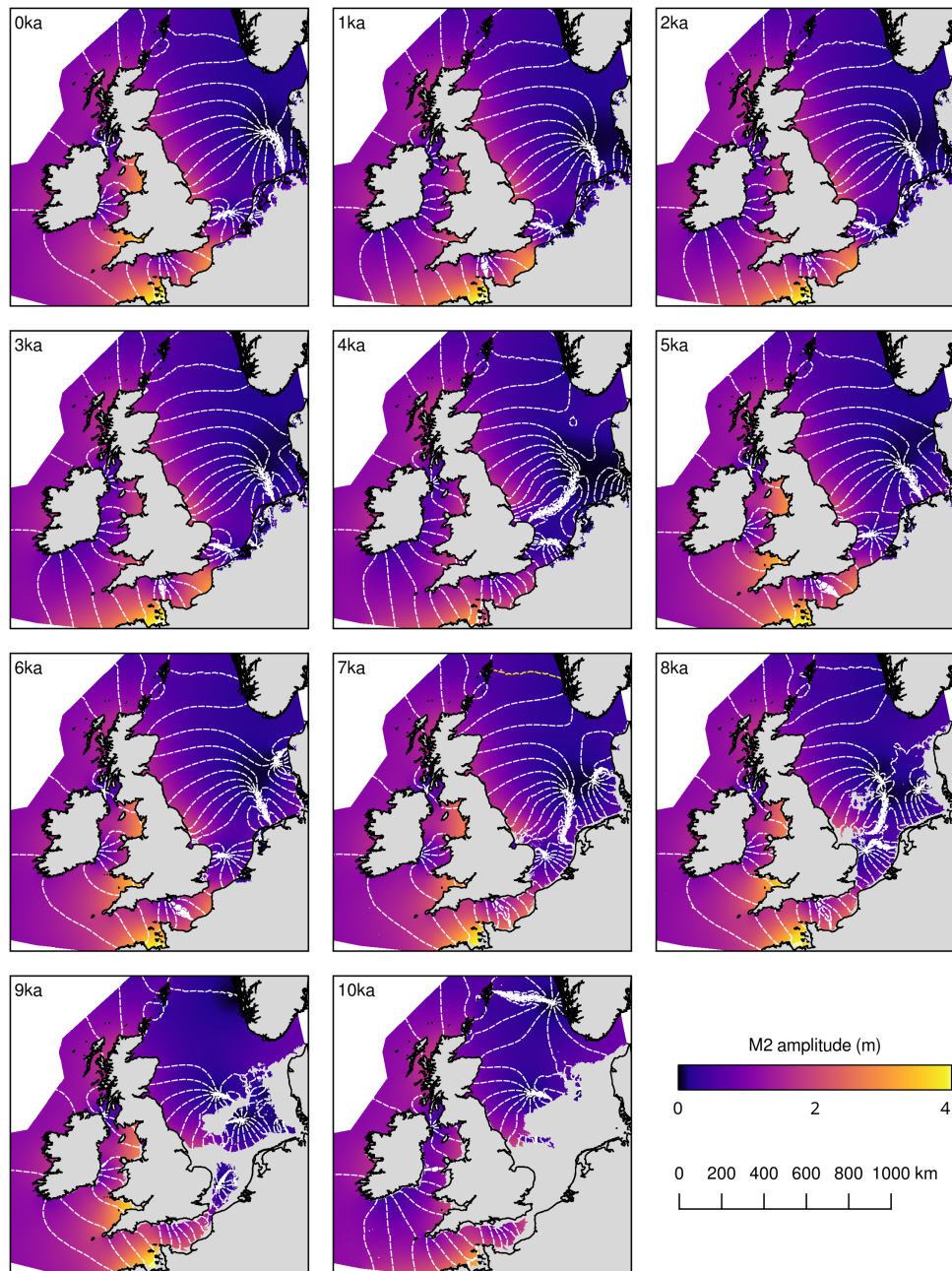


Figure 5. M₂ amplitude (colour bar) and phase (contour lines) for each of the time slices from present day to 10 ka. Grey shading indicates land and the modern coastline is shown in a thick black line.

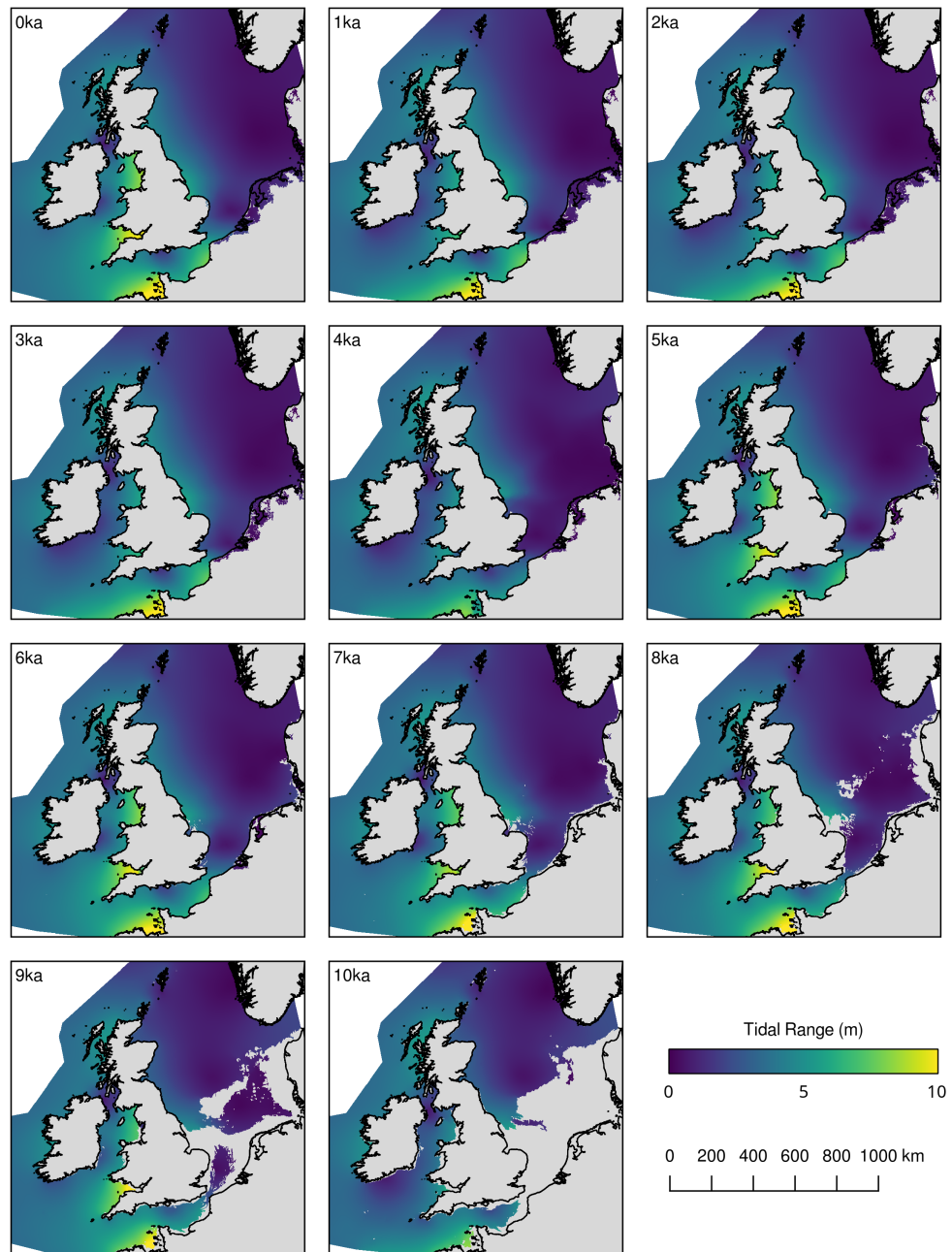


Figure 6. Tidal range in the NW European shelf for each timeslice from present day to 10 ka. Add palaeo shorelines. Grey shading indicates land and the modern coastline is shown in a thick black line.

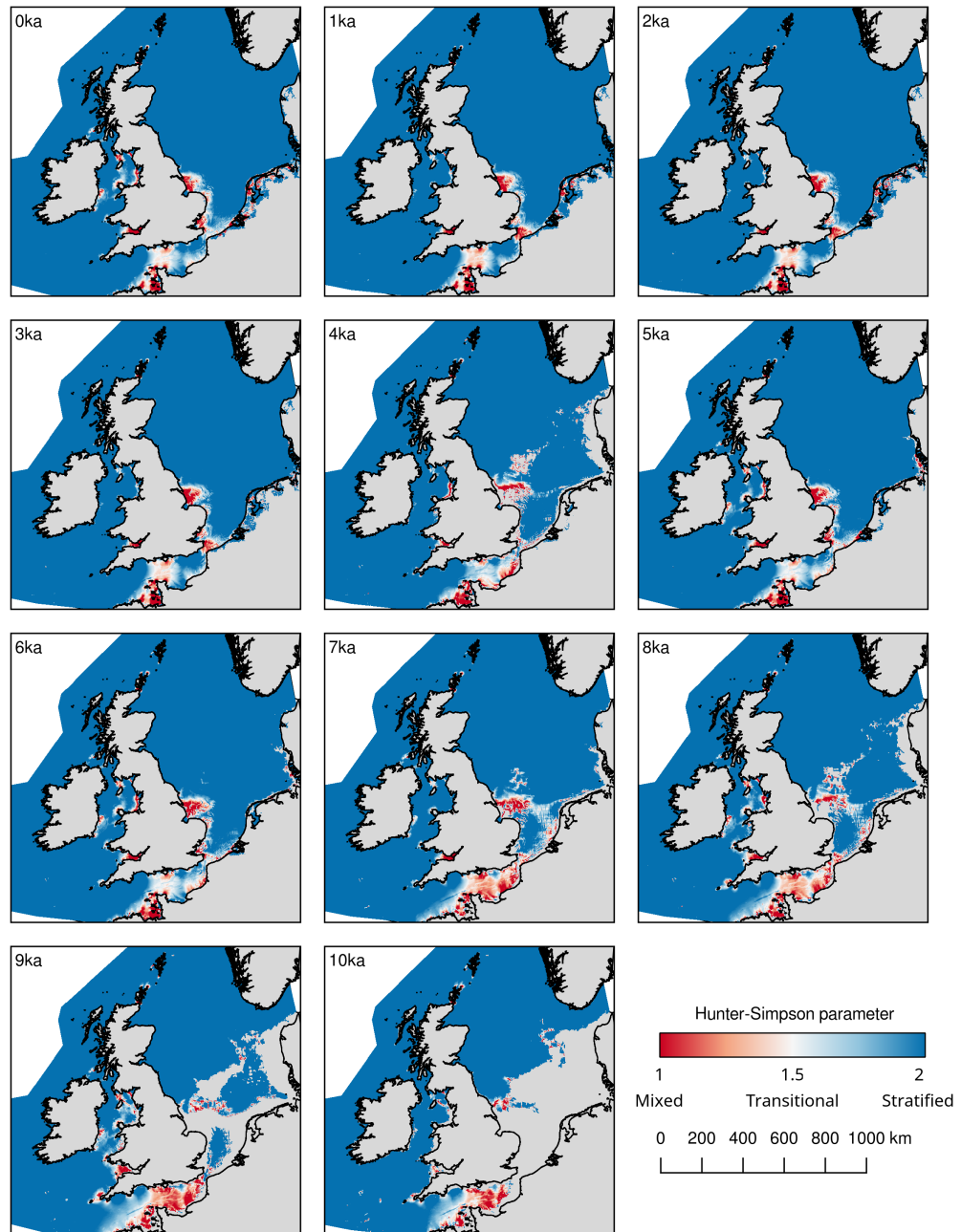


Figure 7. Estimates of the Hunter-Simpson parameter over the last 10,000 years. Blue colours show summer stratification and red show mixed regions. The transition through white colours shows the location of tidal mixing fronts. Grey shading indicates land and the modern coastline is shown in a thick black line.

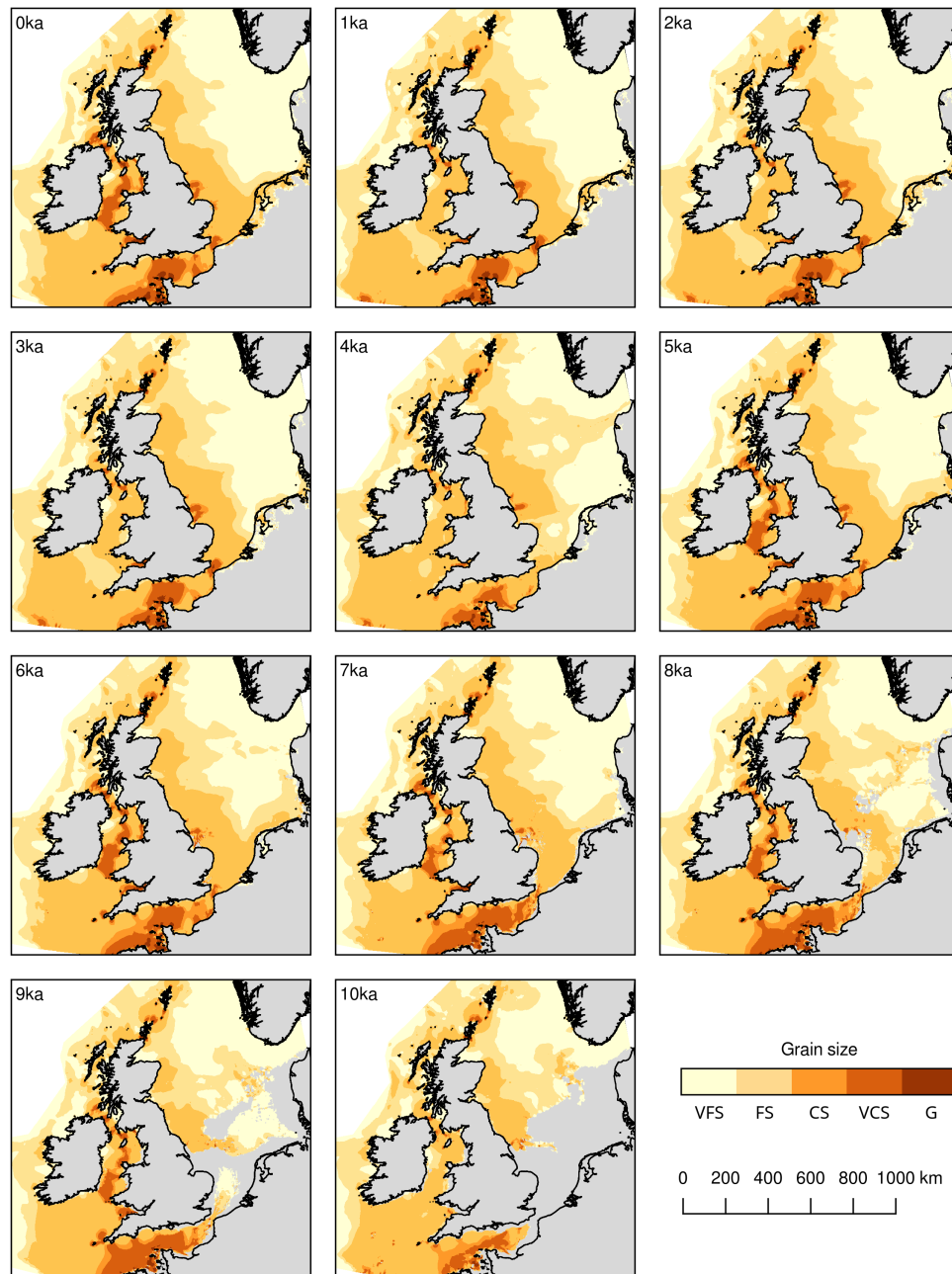


Figure 8. Sediment grain size derived from maximum bed shear stress predicted from the tidal model corrected using the method detailed in [Ward et al. \(2015\)](#). Grey shading indicates land and the modern coastline is shown in a thick black line.